PNAS RESEARCH ARTICLE | ENGINEERING

# Spatially programmed alignment and actuation in printed liquid crystal elastomers

Rodrigo Telles[a], Arda Kotikian[a], Guillaume Freychet[b,1], Mikhail Zhernenkov[b], Patryk Wąsik[b], Benjamin M. Yavitt[b,2], Jorge-Luis Barrera[c], Caitlyn C. Cook[c], Ronald Pindak[b], Emily C. Davidson[d,3], and Jennifer A. Lewis[a,3]

Affiliations are included on p. 7.

Edited by Yonggang Huang, Northwestern University - Evanston, Glencoe, IL; received July 26, 2024; accepted December 12, 2024

**Liquid crystal elastomers (LCEs) exhibit reversible shape morphing behavior when cycled above their nematic-to-isotropic transition temperature. During extrusion-based 3D printing, LCE inks are subjected to coupled shear and extensional flows that can be harnessed to spatially control the alignment of their nematic director along prescribed print paths. Here, we combine experiment and modeling to elucidate the effects of ink composition, nozzle geometry, and printing parameters on director alignment. From rheological measurements, we quantify the dimensionless Weissenberg number (*Wi*) for the flow field each ink experiences as a function of printing conditions and demonstrate that *Wi* is a strong predictor of LCE alignment. We find that director alignment in LCE filaments printed through a tapered nozzle varies radially when $Wi < 1$, while it is uniform when $Wi \gg 1$. Based on COMSOL simulations and in operando X-ray measurements, we show that LCE inks printed through nozzles with an internal hyperbolic geometry exhibit a more uniform director alignment for a given *Wi* compared to those through tapered nozzles. Concomitantly, the stiffness along the print direction and actuation strain of printed LCEs increases substantially under such conditions. By varying *Wi* during printing through adjusting the flow rate "on the fly", LCE architectures with uniform composition, yet locally encoded shape morphing transitions can be realized.**

liquid crystal elastomers | 3D printing | in operando X-ray scattering

## Significance

Aligned liquid crystal elastomers (LCE) are soft materials that exhibit reversible actuation akin to human muscles when thermally cycled above their nematic-to-isotropic transition temperature. Here, we report the effects of LCE ink composition, nozzle geometry, and printing parameters on director alignment. By combining rheological measurements, in operando microbeam X-ray scattering, and simulation, we show that the dimensionless Weissenberg (*Wi*) number, which characterizes ink flow through tapered and hyperbolic nozzles, directly correlates with director alignment in printed LCE filaments. By altering the value of *Wi* on-the-fly during printing, one can fabricate monolithic LCE actuators with spatially programmable alignment, stiffness, and shape morphing behavior.

Liquid crystal elastomers (LCEs) are soft active materials that may find potential application as artificial muscles, mechanologic elements, and soft robotics (1–7). LCEs consist of lightly cross-linked polymer networks composed of either main-chain (8) or side-chain polymers (9)—with rigid mesogens along or pendant to the polymer backbone, respectively. Molecular ordering gives rise to their reversible contractile actuation along their alignment direction, when they are heated above their nematic-to-isotropic transition temperature ($T_{NI}$) (8–10), exposed to light (2, 11, 12), or swelled by solvent (13–15). Several methods have emerged to locally program director alignment, including command surfaces (8), applied magnetic fields (16–19), and extrusion-based 3D printing (5, 20–23). Command surfaces are well suited for encoding complex director alignment in thin LCE films (~ 50 mm thick), while applied magnetic fields can be used to align side-chain LCEs. By contrast, extrusion-based 3D printing enables the rapid design and fabrication of main-chain LCEs, which exhibit the highest contractility. However, the complex interplay between nozzle geometry, printing parameters, and LCE director alignment remains poorly understood.

To date, theoretical models developed for describing flow-induced alignment in liquid crystals (24–26) and rod-like polymers (27, 28) have largely focused on dilute lyotropic systems in weak deformation fields (29). In recent experiments, Hausmann et al. (30) used polarized optical microscopy to quantify alignment during capillary flow of highly concentrated inks containing rod-like particles. They observed that cylindrical filaments composed of a poorly aligned core and highly aligned shell form when subjected to pure shear flow. By introducing extensional flow, they could generate filaments with more uniform alignment. Other researchers have shown that optical birefringence increases when liquid crystal polymers are subjected to extensional flow (31, 32). They posit that shear flow breaks up domains into smaller ones that can rotate and align, while extensional flow promotes further domain alignment via elongation and coalescence (33).

Here, we use an extrusion-based 3D printing method, known as high operating temperature direct ink writing (HOT-DIW) (5), to spatially program director alignment in LCEs (Fig. 1). Specifically, we investigate the role of ink composition and rheology, nozzle geometry, and printing parameters on LCE alignment. Rheology measurements carried out on three different ink compositions are used to understand the effects of complex flow

The authors declare no competing interest.

This article is a PNAS Direct Submission.



[1]Present address: Université Grenoble Alpes, CEA, Leti, Grenoble F-38000, France.

[2]Present address: Department of Chemical and Environmental Engineering, University of Cincinnati, Cincinnati, OH 45221.

[3]To whom correspondence may be addressed. Email: edavidson@princeton.edu or jalewis@seas.harvard.edu.

This article contains supporting information online at https://www.pnas.org/lookup/suppl/doi:10.1073/pnas.2414960122/-/DCSupplemental.

Published January 15, 2025.

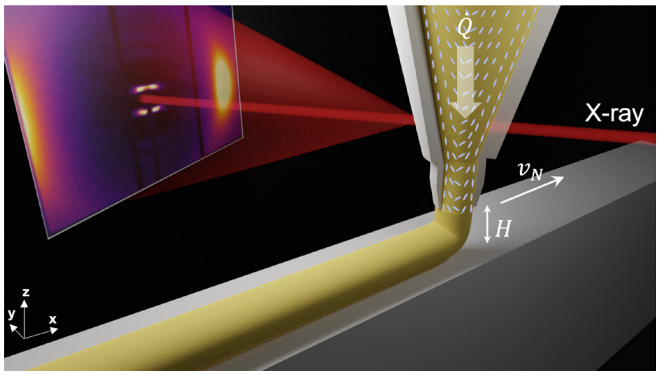


**Fig. 1.** LCE alignment via microbeam WAXS. Spatially tunable alignment is programmed into single filaments by printing LCE inks at controlled flow strengths, determined by the volumetric flow rate ($\dot{Q}$), print height ($H$), and print speed ($v_N$). During printing, a polydomain LCE ink is aligned via shear and extensional forces within the nozzle which is probed via microbeam (2.1 μm × 25 μm) WAXS.

present within the nozzle during printing. Next, we use microbeam wide-angle X-ray scattering (WAXS) to elucidate printing effects on the director alignment both across and along printed LCE filaments. Finally, we print single LCE filaments with tunable stiffness and actuation strain as well as thick LCE sheets with complex shape morphing behavior by locally varying printing conditions, and hence, director alignment.

## Results and Discussion

To achieve programmable director alignment, we equipped a customized HOT-DIW printhead with nozzles composed of either a tapered or hyperbolic internal geometry with an exit inner diameter of $d(z=0)=d_N$ (*SI Appendix*, Fig. S1). This printhead is mounted on a 3-axis, motion-controlled stage that controls translation velocity ($v_N$) and print height ($H$) with high precision. A constant inlet pressure is used to drive LCE ink extrusion at a constant volumetric flow rate ($\dot{Q}$) during printing resulting in a complex flow field. The volumetric flow rate is related to the average ink extrudate velocity ($\langle v \rangle$) by nozzle cross-sectional area $\dot{Q} = \langle v \rangle \pi {d_N}^2/4$. Within each nozzle, shear flow dominates along the walls, while extensional flow dominates along the centerline in regions of nonconstant radius. Hence, subfilament director alignment depends on both the localized shear and extensional deformation flow fields generated during printing. The local flow strength within each nozzle during printing can be quantified through the magnitude of the velocity gradient tensor ($|\nabla \boldsymbol{v}|$), which in our study was approximated at the nozzle outlet. Since shear flow dominates in this region, the flow strength is defined as the shear rate experienced at the walls $|\nabla \boldsymbol{v}| \approx \dot{\gamma}$. The shear rate determines the local ink viscosity, as described by the Carreau fluid model (34):

$$\eta = \eta_0 \left[1 + (\lambda \dot{\gamma})^2\right]^{\frac{n-1}{2}}, \qquad [1]$$

where $\eta$ is the apparent viscosity, $\eta_0$ is the zero-shear viscosity, $\lambda$ is the longest relaxation time for the ink, and $n$ is the flow behavior index (reflecting the degree of shear thinning). Recognizing two distinct time scales associated during extrusion—an inverse shear rate or flow alignment time ($1/\dot{\gamma}$) and an average residence time of the LCE ink in the nozzle ($\tau$)—we define the dimensionless Weissenberg ($Wi = \lambda\dot{\gamma}$) and Deborah ($De = \lambda/\tau$) numbers. The Weissenberg and Deborah numbers indicate the relative contributions of the characteristic polymer relaxation time to flow alignment time and residence time, respectively. For our analysis, we are interested in correlating flow-induced alignment to flow strength as measured by $\dot{\gamma}$ —hence, we use $Wi$. Note that the $De$ would also be valid since it is related to $Wi$ by a geometric factor for confined geometries (35). Furthermore, the Ericksen ($Er = 4\eta\dot{Q}/Kd$) number is another important dimensionless quantity used to characterize the relative magnitude of viscous-to-Frank elastic torques—quantified by the Frank elastic constant $K$—in the flow of nematic fluids (24–26). A small ($Er \ll 1$) and large ($Er \gg 1$) Ericksen number suggests the director is dominated by free energy effects or follows the local flow orientation, respectively. In our system, even for the slowest of flow rates, we find $Er \gg 1$ (see *SI Appendix* for details). Given that the shear and extensional flow field within each nozzle depends on the ink rheology, nozzle geometry, and printing parameters, a detailed understanding of their complex interplay is needed.

Toward that goal, we first measured the LCE ink rheology under shear flow for inks with varying mesogen-to-chain extender ratios. Specifically, we synthesized LCE inks with stoichiometric ratios of 1.30:1, 1.10:1, and 1.02:1 that possess number-averaged molecular weights of 6 kDa, 8 kDa, and 10 kDa, respectively (*SI Appendix*, Fig. S2). Their $T_{NI}$ values, determined by differential scanning calorimetry (DSC), lie within a narrow range from 87 °C to 95 °C (*SI Appendix*, Fig. S2). These inks exhibit three distinct regimes under shear flow. For the 1.30:1 ink, we observe an initial plateau region ($\dot{\gamma} \sim 10^{-2} - 10^{-1}\ s^{-1}$) attributed to rotation of nematic domains along the flow direction, the second plateau region ($\dot{\gamma} \sim 10^{-1} - 10^{1}\ s^{-1}$) is due to the domain breakup, and a shear thinning region ($\dot{\gamma} > 10\ s^{-1}$) due to polymer chains uncoiling (Fig. 2*A*) (33, 36). Similar behavior is observed for both the 1.10:1 and 1.02:1 inks, when accounting for their increased relaxation times. Given that the inks experience shear rates ranging from 1 $s^{-1}$ to 1,000 $s^{-1}$ during printing, we chose only capture the second plateau and shear thinning regions and modeled their behavior as Carreau fluids (Fig. 2*A*). As expected, LCE inks composed of higher MW oligomers exhibit longer relaxation times at a given shear rate, while their relaxation times exhibit an Arrhenius-like dependence on temperature ranging from ~$10^{-2}$ s to $10^{0}$ s (Fig. 2*B* and *SI Appendix*, Fig. S3).

To mechanistically connect printing parameters to liquid crystal alignment, we must estimate the nominal shear rate experienced during printing. We generated a calibration curve for volumetric flow rate as a function of ink composition, printing temperature, and pressure (Fig. 2*C*) in tapered nozzles with diameters of 250 μm and 700 μm (*SI Appendix*, Fig. S4). As the ink flows through each nozzle, the maximum shear rate at the walls is estimated by

$$\dot{\gamma}_{max} \approx \frac{3n+1}{4n}\frac{32\dot{Q}}{\pi d_N^3}. \qquad [2]$$

We identified target shear rate values that result in a polydomain ($\dot{\gamma} < \lambda^{-1}$ or $Wi_{max} < 1$) or approach monodomain ($\dot{\gamma} > \lambda^{-1}$ or $Wi_{max} > 1$) alignment (Fig. 2 *A* and *B*)—providing a means for tuning director alignment using a single monolithic LCE ink, where $Wi_{max}$ is determined by the maximum shear rate at the nozzle wall before the ink exits the nozzle.

In melt-extrusion processes like fiber spinning, one defines a draw ratio ($D_R$) to quantify the effect of extensional flow—i.e., $D_R > 1$ results in filament stretching. Similarly, we can define a draw ratio for extrusion-based 3D printing, where $D_R = v_N/\langle v \rangle$, where $v_N$ is the translational printing speed and $\langle v \rangle$ is the average ink extrudate velocity at the nozzle exit. To introduce extensional flow during printing, we match the printing and extrudate ink speeds and then

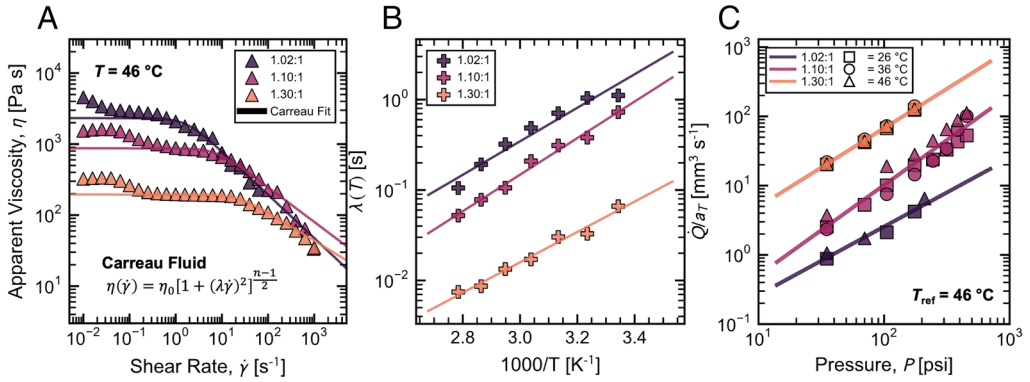


**Fig. 2.** Rheological LCE ink characterization. (*A*) Plot of apparent shear flow viscosity as a function of shear rate fitted with Carreau fluid model for different ink molecular weights, and (*B*) corresponding relaxation times as a function of inverse temperature. (*C*) Temperature-shifted volumetric flow rate calibration map as a function of printing pressure from timed extrusions with a 700 μm tapered nozzle and reference temperature of 46 °C.

decrease the nozzle height. In this case, the true strain experienced by the ink filament during printing is given by Eq. **3**:

$$\epsilon = \frac{v(z)}{\langle v \rangle} = \exp\left[\frac{z}{H} ln(D_R)\right], \qquad [3]$$

where $z$ is the offset height between the nozzle ($z = 0$) and the substrate ($z = -H$) (37, 38). Using the volumetric flow rate calibration map, we quantify the ink extrudate speed for a given nozzle geometry. Unless specified otherwise, all measurements are carried out for $D_R = 1$.

To quantify the local flow strength as a function of position within the printing nozzle, we developed a COMSOL simulation. For our first model, we simulated low and high $Wi_{max}$ number flow through a tapered nozzle (Fig. 3*A*). The ink flow is modeled as a pseudosteady Stokes flow since $Re/Sr \ll 1$, corresponding to the Reynolds ($Re$) and Strouhal ($Sr$) numbers (*SI Appendix*, *Supporting text*), respectively (39). The target $Wi_{max}$ number can be determined by calculating the required volumetric flow rate using Eq. **2**. Moreover, the local LCE ink rheology is modeled using the Carreau fluid fits Eq. **1** from Fig. 2*A*. Notably, the extensional components of flow are estimated from shear measurements in our model. While this is not quantitatively accurate, it gives a reasonable qualitative estimate of the local extensional flow in the nozzle. The ability to perform high-throughput measurements of a full shear and extensional flow field would dramatically improve our ability to model and optimize manufacturing flows of complex fluids (40, 41). By plotting the local $Wi$ number within the tapered nozzle (Fig. 3 *A*, *i* and *iii* and *SI Appendix*, Fig. S5), we find $Wi_{max} = 0.5$ resulted predominantly in $Wi < 1$, whereas increasing $Wi_{max}$ to 500 resulted in $Wi \gg 1$ throughout. As expected, in both cases, there is a negligible contribution of extensional strain within regions of pure capillary flow (i.e., constant radius regions). Next, we designed nozzles with an internal hyperbolic geometry (Fig. 3*B* and *SI Appendix*, Fig. S1). Their hyperbolic curvature results in a nonconstant and monotonically decreasing radius. More importantly, the radius is given by $R^2z$ = constant (42) which has been shown to generate a persistent average extensional strain rate along the centerline ($\tilde{r} = r/d_N = 0$) (43, 44). The increased extensional strain results in more uniform $Wi$ maps for both low and high $Wi_{max}$ (Fig. 3 *B*, *i* and *iii*).

Informed by our COMSOL analysis, we performed in operando microbeam WAXS measurements to map out the local director orientation and average degree of order within each nozzle (*SI Appendix*, Fig. S6). To avoid undesired absorption and scattering from the stainless-steel nozzles, we used projection microstereolithography to fabricate a polymer resin replicate of this commercial tapered nozzle as well as a custom hyperbolic nozzle. X-ray scattering through empty nozzles devoid of LCE ink revealed a slight signal overlap near the liquid crystal nematic peak, $q \approx 1.34$ Å$^{-1}$. These measurements are used for background subtraction (*SI Appendix*, Fig. S7), which is critical for accurately calculating the scalar orientational order parameter, $S = \langle P_2(cos\chi)\rangle$. $S$ has a value of 0 for random orientation and 1 for perfect alignment along the flow direction. Although nematic order is a tensor, for brevity we report a scalar value of $S$ as an average over many domains captured within the scattering volume. The LCE director alignment is calculated by azimuthally averaging the WAXS pattern between a $q$-range of 0.8 to 2.1 Å$^{-1}$ (*SI Appendix*, Fig. S8).

For each nozzle, a map of the orientational order parameter map is calculated (Fig. 3 *A*, *ii* and *iv* and *B*, *ii* and *iv*) and compared to the local flow strength (Fig. 3 *A*, *i* and *iii* and *B*, *i* and *iii*). For both nozzle geometries, director alignment is at a maximum at the nozzle walls, where the contribution of shear to the flow field is highest. Likewise, along the centerline ($\tilde{r} = 0$), alignment increases throughout the radially varying region in both nozzles, reflecting the increasing extensional strain the ink experiences as it passes through a converging region. Importantly, when matching $Wi_{max}$ in the tapered and hyperbolic nozzles, the hyperbolic nozzle induces significantly greater alignment. This difference is particularly dramatic at low $Wi_{max}$ ($Wi_{max} = 0.5$). Given that low $Wi$ printing generally leads to fewer flow instabilities upon extrusion, the ability to achieve strong and uniform alignment at low-to-moderate $Wi$ using hyperbolic nozzles will enhance the robustness and reliability of LCE 3D printing.

High $Wi$ ink flow can induce flow instabilities within the tapered nozzle, which are not observed in the hyperbolic nozzle. WAXS patterns collected at the centerline show an azimuthally sharpening nematic peak as the ink is extruded through the nozzle; this sharpening occurs higher upstream for the hyperbolic nozzle when compared at identical $Wi_{max}$ (Fig. 3*C*). We find that the sharp contraction transition between the tapered and capillary region in the tapered nozzle results in a decrease in centerline alignment that fails to fully recover as the ink continues flowing though the capillary region. This loss of alignment at the tapered-to-capillary transition is observed for both low and high $Wi_{max}$ (Fig. 3*D*, circles) and contributes to the core-shell structure observed in filaments printed from tapered nozzles. This effect is further corroborated by observing the locally probed nematic director orientation within the nozzles, which briefly deviates from the flow direction at the centerline following the transition from the tapered to capillary region (*SI Appendix*, Fig. S9). The nematic director orientation and orientation angle is expressed by a vector field illustrated over the nozzle.

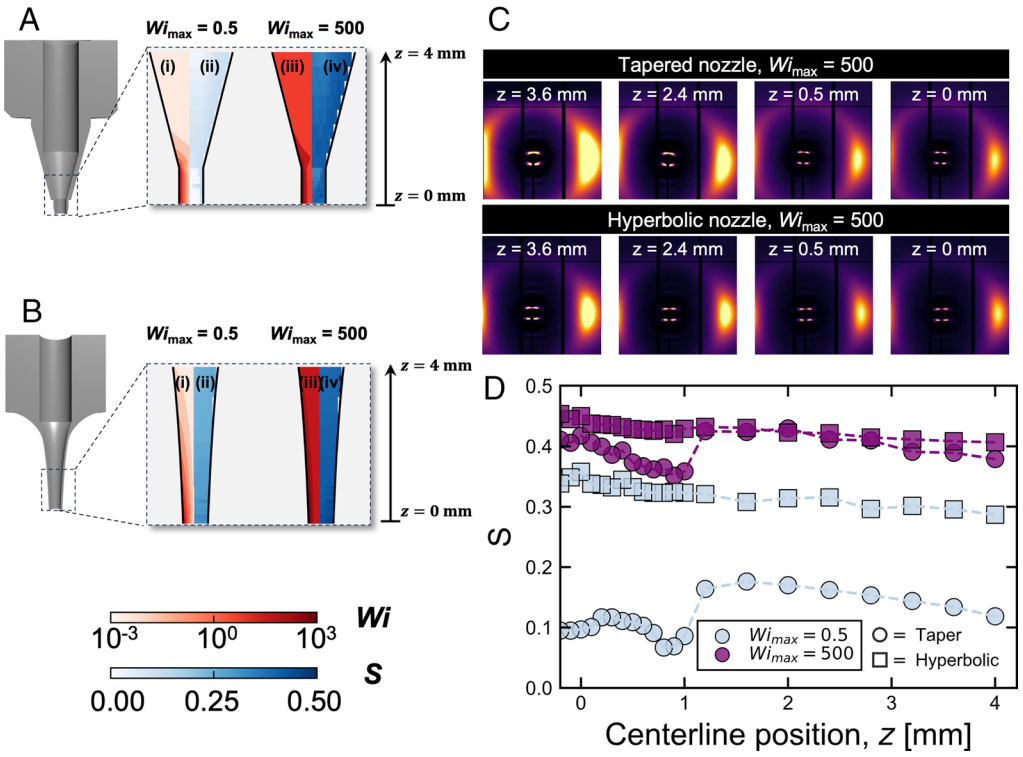


**Fig. 3.** In operando alignment and simulated local flow strengths during 3D printing. (*A*) Schematic of a tapered nozzle (*Left*) and corresponding experimental alignment map (*i* and *iii*, *S*) and simulated local *Wi* map (*ii* and *iv*) for low alignment ($Wi_{max}$ = 0.5) and high alignment ($Wi_{max}$ = 500) conditions as a function of *z*. (*B*) Similarly, results for a hyperbolic nozzle (*Left*) and corresponding experimental alignment and simulated local *Wi* map. (*C*) Centerline *q*-space scattering patterns measured for tapered nozzle with at $Wi_{max}$ = 500 (*Top*) and hyperbolic nozzle, $Wi_{max}$ = 500 (*Bottom*). (*D*) Plot of centerline orientational order parameter as a function of axial position, *z*, for tapered and hyperbolic nozzles, with dotted lines representing average orientational order parameters of ex-situ samples. The data reported were obtained from a 1.10:1 ink printed with a 700 μm tapered nozzle.

To investigate in-nozzle flow effects, we used microbeam WAXS to probe the structure of printed LCE filaments. Single filaments are printed at temperatures between $T_g$ and $T_{NI}$ using HOT-DIW (Fig. 4*A*) and cross-linked with in situ ultraviolet (UV) light. The print conditions were varied to create filaments across ~3 orders of magnitude difference from $Wi_{max}$ ranging from 0.5 to 500. By measuring the distribution of mesogen peaks ($q \approx 1.34$ Å$^{-1}$) radially along a cured filament printed through a tapered nozzle, we identified two filament "states": filaments that form core-shell structures composed of highly aligned edges and low alignment in the core region and uniform filaments. The latter are formed only under high $Wi_{max}$ ($Wi_{max}$ = 500) flow in tapered nozzles (Fig. 4 *B*, *ii*, dark purple circles) or moderate-to-high $Wi_{max} \geq 5$ flow in hyperbolic nozzles (Fig. 4 *B*, *ii*, squares). Core-shell structures are characterized by regions of high alignment at the edges ($\tilde{r} = \pm 0.5$) and low alignment toward the core ($\tilde{r} = 0$) (Fig. 4*B*). Notably regions of low alignment overestimate the degree of order, as the X-ray beam probes two "ordered" regions in addition to the low alignment core when probing along the filament centerline ($\tilde{r} = 0$). The low alignment core is evident by the appearance of a polydomain ring (Fig. 4 *B*, *i*, *Center*) versus anisotropic peaks near the edges (Fig. 4 *B*, *i*, far *Left* and far *Right*). Moreover, a similar effect is observed when comparing scattering patterns obtained for different flow strengths (Fig. 4*C* and *SI Appendix*, Fig. S10). Namely, $Wi_{max}$ = 0.5 results in a polydomain alignment state at the filament core, whereas more uniform alignment occurs with increasing $Wi_{max}$. The maximum average *S* values for LCE filaments printed using tapered and hyperbolic nozzles are roughly 0.45 and 0.47, respectively.

To study the role of subfilament director heterogeneity on mechanical properties, we printed single LCE filaments in tapered nozzles at $Wi_{max}$ = 0.5, 5, 50, and 500. Interestingly, the through-filament averaged orientational order parameter, $S_{bulk}$, is found to follow a sigmoidal relationship with $Wi_{max}$ (Fig. 4*C*). A similar result was found experimentally by Schätzle et al. (45) and theoretically predicted by Fridrickh and Terentjev (46) for uniaxially aligned LCEs generated by mechanical stretching. This relationship holds for different LCEs, nozzle designs, and printing temperatures (*SI Appendix*, Fig. S11). We observed a transition from low $S_{bulk}$ to a plateau value of $S_{bulk} \approx 0.45$ for $Wi_{max} > 1$, whereas for $Wi_{max} < 1$, the poorly aligned core dominates $S_{bulk}$ (Fig. 3 *B, ii*). Hence, the dimensionless $Wi_{max}$ is a strong predictor for degree of alignment in printed LCEs.

To demonstrate the impact of spatially varying alignment on LCE mechanical properties and actuation performance, we printed LCE filaments (25 mm long) using a tapered nozzle diameter of 700 μm, and print conditions that produce $Wi_{max}$ = 0.5, 5, 50, and 500. Tensile measurements reveal that the stiffness of printed LCEs increases with increasing director alignment (Fig. 4*D*, solid lines). However, the width of the soft-elastic plateau and elongation to break decrease with alignment. We attribute these observations to the loss of their soft polydomain core, and increasing thickness of the stiffer aligned shell that limits filament stretchability (47). Notably, even for the slowest flows, a thin aligned shell is present, which likely leads to stress concentration at the boundaries leading to premature fracture upon extension relative to an ideal polydomain filament. This observation is further corroborated when comparing LCE filaments printed with a tapered nozzle versus a hyperbolic nozzle. We find that filaments printed with a hyperbolic nozzle result in an even greater reduction of the soft-elasticity plateau region for $Wi_{max}$ = 0.5 and nearly indistinguishable for $Wi_{max}$ = 500 and reduced elongation to break (Fig. 4*D*, dashed lines).

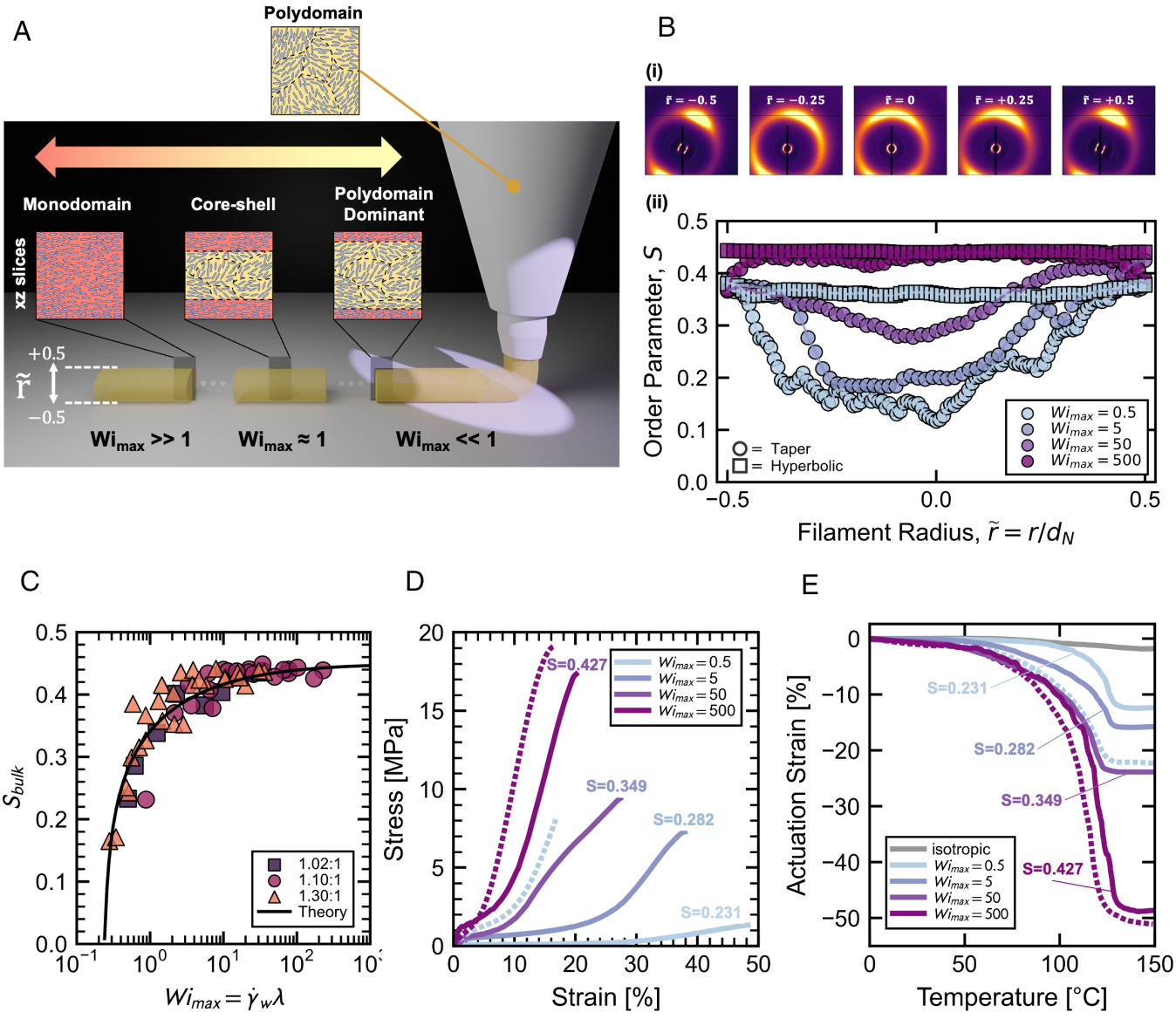


**Fig. 4.** Subfilament director alignment and mechanical properties of printed LCE filaments. (*A*) Schematic of programming LCE alignment on-the-fly. (*B*) Radially resolved alignment in a single LCE filament printed through a 700 μm diameter nozzle at $Wi_{max}$ = 0.5 (*Top* images) via microbeam X-ray scattering (beam size 2.1 μm × 25 μm) and their orientational order parameter plot across filament radius for varying nozzle geometry and $Wi_{max}$ (*Bottom* plot). (*C*) Plot of filament-averaged orientational order parameter as a function of $Wi_{max}$ for LCE filaments printed with different compositions using tapered nozzles of 250 μm or 700 μm in diameter and compared to theory. (*D*) Tensile stress as a function of strain for 1.10:1 LCE filaments printed at varying $Wi_{max}$ through a tapered nozzle (solid line) and hyperbolic nozzle (dashed line). (*E*) Actuation strain of 1.10:1 LCE filaments printed at varying $Wi_{max}$ through a tapered nozzle (solid line) and hyperbolic nozzle (dashed line), as measured parallel to print path from second heating cycle from 0 °C to 150 °C. Data obtained from a 1.10:1 ink printed with a 700 μm tapered nozzle, unless specified otherwise.

Although this limitation is inherent to flow-induced alignment, a simple solution would be to use a custom nozzle amenable to two-phase flow—where a secondary fluid encapsulates the LCE ink and provides a tunable wall slip boundary condition (35)—allowing for the fabrication of filaments with a soft core and shell or a stiff core with a soft shell. Next, we measured their actuation performance using dynamic mechanical analysis (DMA) during thermal cycling between 0 °C and 150 °C (Fig. 4*E*). Upon initial heating above $T_{NI}$, their thermal history is erased. Hence, their contractile actuation strain is reported for the second heating cycle. Improved core alignment within the printed LCE filaments results in a lower actuation temperature and larger actuation strains with a maximum contractile strain of − 48 %. As a comparison, filaments were printed with a 700 μm hyperbolic nozzle for $Wi_{max}$ = 0.5 and 500. We find that filaments printed at $Wi_{max}$ = 500 exhibit similar maximum contractile strains for both hyperbolic and tapered nozzles. By contrast, those printed through the hyperbolic nozzle at $Wi_{max}$ = 0.5 exhibited a much larger contractile response than their tapered nozzle counterparts at the same $Wi_{max}$. To achieve the same director alignment and, hence, contractility, such filaments must be printed through a tapered nozzle at $Wi_{max}$ = 50 (Fig. 4*B*).

As a final demonstration, we printed an LCE structure with spatially programmed director alignment in which topographic features are encoded by printing at low and high *Wi* (Fig. 5 *A, i* and Movie S1). For this, a flat sheet composed of 9 × 6 unit cells (20 mm × 20 mm in a square spiral pattern) is printed (Fig. 5 *A, ii*), in which the unit cells in the "H"-shape region are printed at $Wi_{max}$ = 500 and those in the surrounding regions are printed at $Wi_{max}$ = 0.5. To predict their actuated shape, we used a LCE model implemented in a 3D finite element framework (17, 48). The complete boundary conditions and calibration details are provided in *SI Appendix, Supporting text* and Figs. S12–S14. Their predicted shape change is

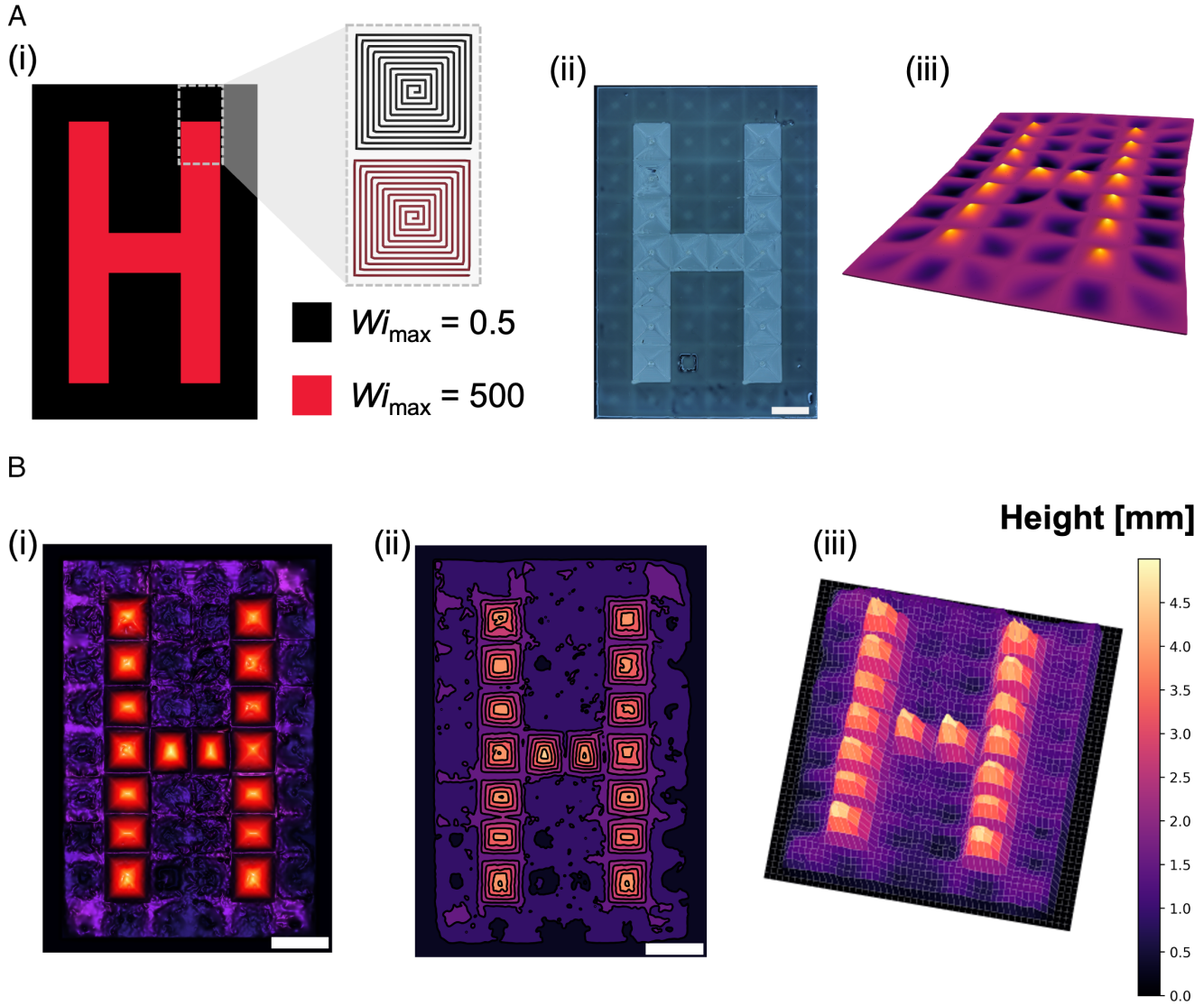


**Fig. 5.** Spatially encoded director alignment in printed LCEs. (*A*) (*i*) Schematic representation of an H-shape composed of low-aligned (black) and highly aligned (red) spiral print paths. (*ii*) Corresponding optical image of H-shape taken at room temperature. (*iii*) Predicted shape change at 150 °C. (*B*) Experimentally observed displacement at 150 °C illustrated as a (*i*) height map, (*ii*) contour plot, and (*iii*) 3D height map. Data obtained from a 1.10:1 ink printed with a 250 μm tapered nozzle (Scale bar, 10 mm).

shown in Fig. 5 *A*, *iii*. Experimentally, when heated above $T_{NI}$, the aligned unit cells printed at $Wi_{max}$ = 500 exhibit a 2D-to-3D shape change, i.e., they morph from a flat sheet to conical surfaces with positive Gaussian curvature, while poorly aligned unit cells printed at $Wi_{max}$ = 0.5 remain relatively flat (Fig. 5 *B*, *i–iii*). An averaged maximum out-of-plane height of 4.5 mm is observed upon heating this printed LCE sheet to 150 °C.

## Conclusion

In summary, we have elucidated the role of ink composition, nozzle geometry, rheology, and printing parameters on LCE director alignment through a combination of experiment and computational modeling. Harnessing this knowledge, we have fabricated LCEs with locally encoded director alignment by varying printing conditions on-the-fly. LCE filaments printed through a hyperbolic nozzle exhibited significantly enhanced and more uniform director alignment than tapered nozzles when compared at the same *Wi*. This work opens broad avenues for rapidly designing and fabricating LCEs with programmed shape morphing and mechanics for use as artificial muscle actuators, mechanologic, and soft robotic systems.

## Materials and Methods

**LCE Ink.** All reagents were used without additional purification unless otherwise noted. The liquid crystalline oligomer ink was synthesized by a one-pot aza-Michael addition synthesis (10). To a 25 mL round bottom flask, the difunctional liquid crystal mesogen 1,4-Bis-[4-(6-acryloyloxyhexyloxy)benzoyloxy]-2-methylbenzene (Synthon, 97%) and n-butyl amine (Sigma-Aldrich, 99.5%) were combined in a 1.02:1, 1.10:1, or 1.30:1 molar ratio with 2 wt% 2,2-dimethoxy-2-phenylacetophenone (Sigma-Aldrich) and 0.2 wt% butylated hydroxytoluene (Sigma-Aldrich). The reaction was heated to 105 °C, covered in aluminum foil, and stirred for 18 h with a PTFE-coated stir bar.

**Gel Permeation Chromatography (GPC).** LCE molecular weights were determined via GPC with HPLC grade tetrahydrofuran (Sigma-Aldrich) as the mobile phase on a Wyatt Technology chromatograph equipped with an in-line multiangle light scattering detector, viscometer, and refractive index detector. First, a sample was dissolved in THF to a final concentration of 3.0 to 3.2 mg/mL. Samples were stirred for at least 16 h before measurement. The solution was filtered through

a 0.2 μm syringe filter. Then, 100 μL of sample was injected into a set of four columns (Agilent PL-Gel 10 μm mixed B). The Mark–Houwink–Sakurada method was used for molecular weight calculations.

**DSC.** Samples for DSC were prepared by loading ~10 mg of polymer sample in Tzero aluminum hermetic pans. Under nitrogen flow, the polymers were heated to 150 °C to erase any thermal history, held for 10 min, followed by two cycles of cooling to −50 °C and heating to 150 °C at a ramp rate of 10 °C $min^{-1}$ (DSC 2500, TA Instruments). The data from the second heating cycle were used for analysis.

**Rheology.** Rheological properties of the LCE inks were characterized using a controlled stress rheometer (Discovery HR-2 Hybrid Rheometer, TA Instruments) equipped with a 20 mm steel Peltier parallel plate geometry and a 0.250 mm gap. Prior to testing, the ink was brought above the $T_{NI}$ to erase thermal history and then cooled to the temperature of interest. Viscosity measurements were recorded with an equilibration time equal to the LCE ink residence time within the nozzle.

**3D Printing.** LCE inks were printed using a custom HOT-DIW setup (5). Briefly, a machined copper block with an RTD sensor (Omega) and two 100-watt cartridge heaters (Omega) provide closed-loop temperature control via an Omega platinum series single-zone temperature controller. Ink was loaded into a 3 cc stainless steel barrel with a 50 μm, 250 μm, or 700 μm stainless steel nozzle (Tecdia), or a custom projection microstereolithography printed tapered or hyperbolic nozzle (microArch® S240, Boston Micro Fabrication), coupled to a Nordson 3 cc high-pressure adapter (Nordson). The printhead was mounted onto a custom three-axis motion control stage (Aerotech Inc.) that uses an Ultimus V pressure box (Nordson) to deposit LCE ink. Printing heights are set equal to the diameter of the nozzle and printing speeds are set to match the ink extrudate velocity, unless otherwise specified. During printing, filaments are cured in situ (Omnicure S2000 with 320 to 500 nm filter, Excelitas) at 12 mW $cm^{-2}$ (PM100D, ThorLabs), followed by a 30-min postcure on each side at 12 mW $cm^{-2}$ (XYZprinting, Inc).

**Actuation Measurements.** Cyclic actuation measurements were performed using a dynamic mechanical analyzer (Q850, TA Instruments) equipped with an ACS-3 refrigerated air supply using the controlled force method. To prevent premature failure at the sample-DMA clamp interface, gripping tabs were created by submerging the ends of ~15 mm test filaments into a stiff UV curable resin (HTL resin, BMF3D) contained within a 3D-printed (High Temp resin, Form3 printer) rectangular gripping cap, and then UV cross-linking the stiff resin (*SI Appendix*, Fig. S15). Using a 0.01 N preload and 0 N dynamic force during testing, samples were heated to 150 °C to erase thermal history, held for 5 min, cooled to 0 °C, and heated to 150 °C at a ramp rate of 10 °C $min^{-1}$. Data shown from second heating cycle.

**Mechanical Testing.** Stress–strain tests were performed on an Instron 5943 with a 1 kN load cell and equipped with fiber filament tensile grips at 50 μm $s^{-1}$. Sample dimensions were measured before each test after thermally cycling filaments above $T_{NI}$ to remove any thermal history.

**WAXS.** X-ray measurements were performed in transmission mode on the Soft Matter Interfaces (SMI) beamline 12-ID at the National Synchrotron Light Source II (NSLS-II). Scattering patterns were measured at 16.1 keV with a microfocused beam spot size of 2.1 μm × 25 μm (vertical × horizontal), exposure time of 0.2 s, and recorded on a Pilatus 300 K-W or 900 K-W detector (Dectris). Ex-situ measurements were performed under vacuum by affixing LCE single filaments to a laser-cut acrylic sheet with 10 × 15 grid of 2 mm diameter holes. In operando measurements were performed in air by mounting our custom HOT-DIW printhead onto a printbed with independent *x*, *y*, and *z* control. The printbed apparatus is detailed in previous work by Wiegart et al. (49). In-air or empty nozzle measurements were collected and used for background subtraction. All analysis presented used a single "stitched" scattering pattern, composed of measurements collected at multiple detector angles to cover a wider range of reciprocal space. Scalar orientational order parameters, $S = \langle P_2(cos\chi)\rangle$, were calculated by extracting the mesogen scattering peak intensity (0.8 to 2.1 $Å^{-1}$) as a function of azimuthal angle. Data processing and stitching were performed using custom Python scripts based on pyFAI (50) and the SMI beamline analysis package (51).

**COMSOL.** To quantify the local flow strength inside the nozzle during printing, numerical simulations were performed with COMSOL Multiphysics v6.1 (Dassault Systèmes, Waltham, MA) for laminar Stokes-flow conditions with gravity effects included. The experimentally determined ink density and viscosity were used to estimate a Reynolds number, $Re \ll 1$, confirming laminar flow conditions.

**Topographical Measurements.** Topographical height maps were recorded and stitched using a Keyence VHX-7000 equipped with a VHX-E20 objective. Printed H-shape sheet was placed on a thin silicone oil layer on top of a custom-built, heated anodized aluminum stage.

**Data, Materials, and Software Availability.** Data from this study are available on the Materials Data Facility at https://doi.org/10.18126/xy1k-q029 (52).

**ACKNOWLEDGMENTS.** We gratefully acknowledge support from the NSF through the Harvard MRSEC (DMR-2011754) and the ARO MURI program (W911NF-22-1-0219). This work was performed in part under the auspices of the US Department of Energy by Lawrence Livermore National Laboratory under contract DE-AC52-07NA27344, LDRD tracking number 22-ERD-030, and release number LLNL-JRNL-866163. This research used the Soft Matter Interfaces (SMI) beamline 12-ID of the National Synchotron Light Source II, a U.S. Department of Energy (DOE) Office of Science User Facility operated for the DOE Office of Science by Brookhaven National Laboratory under Contract No. DE-SC0012704. The X-ray scattering computations were run on the FASRC Odyssey and Cannon clusters supported by the FAS Division of Science Research Computing Group at Harvard University. We thank Dr. Colin Loeb for running GPC and Dr. Lutz Wiegart for developing the in-line translation stage used at SMI 12-ID.

Author affiliations: [a]John A. Paulson School of Engineering and Applied Sciences and Wyss Institute for Biologically Inspired Engineering, Harvard University, Cambridge, MA 02138; [b]Complex Scattering Program, National Synchrotron Light Source II, Brookhaven National Laboratory, Upton, NY 11973; [c]Materials Engineering Division, Lawrence Livermore National Laboratory, Livermore, CA 94550; and [d]Department of Chemical and Biological Engineering, Princeton University, Princeton, NJ 08544

Author contributions: R.T., E.C.D., and J.A.L. designed research; R.T., A.K., G.F., M.Z., P.W., B.M.Y., J.-L.B., and E.C.D. performed research; C.C.C. and R.P. contributed new reagents/analytic tools; R.T. and E.C.D. analyzed data; and R.T., E.C.D., and J.A.L. wrote the paper.

1. A. Kotikian *et al.*, Innervated, self-sensing liquid crystal elastomer actuators with closed loop control. *Adv. Mater.* **33**, 2101814 (2021).
2. S. Palagi *et al.*, Structured light enables biomimetic swimming and versatile locomotion of photoresponsive soft microrobots. *Nat. Mater.* **15**, 647 (2016).
3. M. Rogóż, H. Zeng, C. Xuan, D. S. Wiersma, P. Wasylczyk, Light-driven soft robot mimics caterpillar locomotion in natural scale. *Adv. Opt. Mater.* **4**, 1689–1694 (2016).
4. A. Kotikian *et al.*, Untethered soft robotic matter with passive control of shape morphing and propulsion. *Sci. Rob.* **4**, eaax7044 (2019).
5. A. Kotikian, R. L. Truby, J. W. Boley, T. J. White, J. A. Lewis, 3D printing of liquid crystal elastomeric actuators with spatially programed nematic order. *Adv. Mater.* **30**, 1706164 (2018).
6. M. J. Ford *et al.*, Movement with light: Photoresponsive shape morphing of printed liquid crystal elastomers. *Matter* **7**, 1207–1229 (2024).
7. C. Yuan *et al.*, 3D printed reversible shape changing soft actuators assisted by liquid crystal elastomers. *Soft Matter* **13**, 5558–5568 (2017).
8. T. H. Ware, M. E. McConney, J. J. Wie, V. P. Tondiglia, T. J. White, Voxelated liquid crystal elastomers. *Science* **347**, 982–984 (2015).
9. J. Küpfer, H. Finkelmann, Nematic liquid single crystal elastomers. *Die Makromol. Chem. Rapid Commun.* **12**, 717–726 (1991).
10. T. Ware, T. White, Programmed liquid crystal elastomers with tunable actuation strain. *Polym. Chem.* **6**, 4835–4844 (2015).
11. Y. Yu, M. Nakano, T. Ikeda, Directed bending of a polymer film by light. *Nature* **425**, 145–145 (2003).
12. A. W. Hauser, D. Liu, K. C. Bryson, R. C. Hayward, D. J. Broer, Reconfiguring nanocomposite liquid crystal polymer films with visible light. *Macromolecules* **49**, 1575–1581 (2016).
13. K. D. Harris, C. W. M. Bastiaansen, D. J. Broer, Physical properties of anisotropically swelling hydrogen-bonded liquid crystal polymer actuators. *J. Microelectromech. Syst.* **16**, 480–488 (2007).
14. J. M. Boothby, H. Kim, T. H. Ware, Shape changes in chemoresponsive liquid crystal elastomers. *Sens. Actuators B: Chem.* **240**, 511–518 (2017).
15. D. S. Kim *et al.*, Self-folding liquid crystal network filaments patterned with vertically aligned mesogens. *ACS Appl. Mater. Interfaces* **14**, 50171–50179 (2022).
16. S. Li *et al.*, Liquid-induced topological transformations of cellular microstructures. *Nature* **592**, 386–391 (2021).

17. S. Li *et al.*, Controlling liquid crystal orientations for programmable anisotropic transformations in cellular microstructures. *Adv. Mater.* **33**, 2105024 (2021).
18. S. Li *et al.*, Self-regulated non-reciprocal motions in single-material microstructures. *Nature* **605**, 76–83 (2022).
19. Y. Wang *et al.*, Printing mosaics of magnetically programmed liquid crystal directors for reversibly morphing soft matter. arXiv [Preprint] (2024). http://arxiv.org/abs/2401.06590 (Accessed 3 July 2024).
20. E. C. Davidson, A. Kotikian, S. Li, J. Aizenberg, J. A. Lewis, 3D Printable and reconfigurable liquid crystal elastomers with light-induced shape memory via dynamic bond exchange. *Adv. Mater.* **32**, 1905682 (2020).
21. C. P. Ambulo *et al.*, Four-dimensional printing of liquid crystal elastomers. *ACS Appl. Mater. Interfaces* **9**, 37332–37339 (2017).
22. M. O. Saed *et al.*, Molecularly-engineered, 4D-printed liquid crystal elastomer actuators. *Adv. Funct. Mater.* **29**, 1806412 (2019).
23. K. George *et al.*, 3D printing of responsive chiral photonic nanostructures. *Proc. Natl. Acad. Sci. U.S.A.* **120**, e2220032120 (2023).
24. F. M. Leslie, Some constitutive equations for liquid crystals. *Arch. Ration. Mech. Anal.* **28**, 265–283 (1968).
25. F. M. Leslie, Continuum theory of liquid crystals. *Rheol. Acta* **10**, 91–95 (1971).
26. J. L. Ericksen, Conservation laws for liquid crystals. *Trans. Soc. Rheol.* **5**, 23–34 (1961).
27. R. G. Larson, M. Doi, Mesoscopic domain theory for textured liquid crystalline polymers. *J. Rheol.* **35**, 539–563 (1991).
28. M. Doi, Molecular dynamics and rheological properties of concentrated solutions of rodlike polymers in isotropic and liquid crystalline phases. *J. Polym. Sci.: Polym. Phys. Ed.* **19**, 229–243 (1981).
29. W. R. Burghardt, Molecular orientation and rheology in sheared lyotropic liquid crystalline polymers. *Macromol. Chem. Phys.* **199**, 471–488 (1998).
30. M. K. Hausmann *et al.*, Dynamics of cellulose nanocrystal alignment during 3D printing. *ACS Nano* **12**, 6926–6937 (2018).
31. G. G. Viola, D. G. Baird, Studies on the transient shear flow behavior of liquid crystalline polymers. *J. Rheol.* **30**, 601–628 (1986).
32. Y. Ide, Z. Ophir, Orientation development in thermotropic liquid crystal polymers. *Polym. Eng. Sci.* **23**, 261–265 (1983).
33. S. Onogi, T. Asada, "Rheology and rheo-optics of polymer liquid crystals" in *Rheology*, G. Principles, G. Astarita, L. N. Marrucci, Eds. (Springer, US, 1980), **vol. 1**, pp. 127–147.
34. P. J. Carreau, Rheological equations from molecular network theories. *Trans. Soc. Rheol.* **16**, 99–127 (1972).
35. K. D. Housiadas, A. N. Beris, On the elongational viscosity of viscoelastic slip flows in hyperbolic confined geometries. *J. Rheol.* **68**, 327–339 (2024).
36. R. G. Larson, *The Structure and Rheology of Complex Fluids* (Oxford University Press, 1999).
37. M. A. Matovich, J. R. A. Pearson, Spinning a molten threadline. steady-state isothermal viscous flows. *Ind. Eng. Chem. Fund.* **8**, 512–520 (1969).
38. M. M. Denn, Continuous drawing of liquids to form fibers. *Annu. Rev. Fluid Mech.* **12**, 365–387 (1980).
39. W. M. Deen, *Analysis of Transport Phenomena* (Oxford University Press, ed. 2, 2012).
40. C. D. Young, P. T. Corona, A. Datta, M. E. Helgeson, M. D. Graham, Scattering-informed microstructure prediction during Lagrangian evolution (SIMPLE)–A data-driven framework for modeling complex fluids in flow. *Rheol. Acta* **62**, 587–604 (2023).
41. P. T. Corona *et al.*, Fingerprinting soft material nanostructure response to complex flow histories. *Phys. Rev. Mater.* **6**, 045603 (2022).
42. D. F. James, Flow in a converging channel at moderate reynolds numbers. *AIChE J.* **37**, 59–64 (1991).
43. M. S. N. Oliveira, M. A. Alves, F. T. Pinho, G. H. McKinley, Viscous flow through microfabricated hyperbolic contractions. *Exp. Fluids* **43**, 437–451 (2007).
44. T. J. Ober, S. J. Haward, C. J. Pipe, J. Soulages, G. H. McKinley, Microfluidic extensional rheometry using a hyperbolic contraction geometry. *Rheol. Acta* **52**, 529–546 (2013).
45. J. Schätzle, W. Kaufhold, H. Finkelmann, Nematic elastomers: The influence of external mechanical stress on the liquid-crystalline phase behavior. *Die Makromol. Chem.* **190**, 3269–3284 (1989).
46. S. V. Fridrikh, E. M. Terentjev, Polydomain-monodomain transition in nematic elastomers. *Phys. Rev. E* **60**, 1847–1857 (1999).
47. J. S. Biggins, M. Warner, K. Bhattacharya, Elasticity of polydomain liquid crystal elastomers. *J. Mech. Phys. Solids* **60**, 573–590 (2012).
48. J. L. Barrera, C. Cook, E. Lee, K. Swartz, D. Tortorelli, Liquid crystal orientation and shape optimization for the active response of liquid crystal elastomers. *Polymers* **16**, 1425 (2024).
49. L. Wiegart *et al.*, Instrumentation for in situ/operando X-ray scattering studies of polymer additive manufacturing processes. *Synchrotron Radiat. News* **32**, 20–27 (2019).
50. J. Kieffer, D. Karkoulis, PyFAI, a versatile library for azimuthal regrouping. *J. Phys.: Conf. Ser.* **425**, 202012 (2013).
51. R. J. Pandolfi *et al.*, Xi-cam: A versatile interface for data visualization and analysis. *J. Synchrotron. Rad.* **25**, 1261–1270 (2018).
52. Data set for R. Telles et al., Spatially programmed alignment and actuation in printed liquid crystal elastomers, PNAS, 2025. Materials Data Facility. https://doi.org/10.18126/xy1k-q029. Deposited 20 December 2024.